Arabian Journal for Science and Engineering (2021) 46:1313–1332
https://doi.org/10.1007/s13369-020-05051-y

RESEARCH ARTICLE–ELECTRICAL ENGINEERING

Analysis and Classification of Faults in Switched Reluctance Motors Using Deep Learning Neural Networks

E. Fantin Irudaya Raj[1] · **M. Balaji**[2]

Received: 4 June 2020 / Accepted: 20 October 2020 / Published online: 12 November 2020

Abstract
The simple and robust construction, less weight, wide operating speed range, and higher fault tolerance capability of switched reluctance (SR) motor make it a viable contender for the conventional dc and ac machines. The faults at the rotor, winding, stator converters, and sensors lead to overcurrent, increase torque ripples, and sudden breakdown of the system. Thus, it is an urgent requirement to recognize and classify the faults that exist in switched reluctance motors, thereby the reliability, robustness, and widespread utilization of SR motors can be increased. The phases of the SR Motor are excited by using an asymmetric bridgeless resonance converter. This paper proposes an automatic diagnosis and classification of faults using radial basis function neural network (RBFNN). A mathematical model of the SR motor is established to determine the state of the art of fault condition of SR motors. The speed data of SR motor are utilized by RBFNN to generate fault information. Gabor filter is used for preprocessing the input data, and segmentation is achieved using high accurate DCT-DOST transformation. A gray-level co-occurrence matrix optimized with a genetic algorithm is used to extract the features in the speed signal of the motor. A test setup was developed in MATLAB to measure the performances of the RBFNN classifier in real-time. The effectiveness of the simulated fault classification model is verified by comparing the results of the conventional PI controller with several optimized algorithm-based tuned PI controllers.

Keywords SR motor · Fault classification · Speed control · RBFNN · BR converter · Genetic algorithm

1 Introduction

Switched reluctance motor (SRM) with a large number of promising features like simple construction, less weight, robust, higher torque to inertia ratio, less maintenance requirement, low cost, and wide range of operating speed is a potential candidate for variable speed applications. The salient poles of the stator and rotor of the SR motor are made of steel lamination. The windings are connected in each phase (opposite poles) of the stator with no windings on the rotor. The proper excitation of the current with respect to the position of the rotor decides the performance of SRM. When a current flows in any one of the phases, the torque gets generated due to the rotor movement so as to line up with the energized stator pole. The direction of the generated torque changes due to the rotor motion in accordance with the excited phase and is not a function of the current direction passing in the phase windings. Torque can be generated by synchronizing the excitation of every phase with the position of the rotor. The power electronic devices control the excitation current in the motor winding. The performance and the estimation of the motor drive are determined by the type of converter used. Among the available converter topologies (C-dump, C-dump with a freewheeling transistor, and bridgeless resonance (BR) converters) of SR motor, the bridgeless resonance (asymmetric) power converter is considered in this paper as it offers a much faster rate of fall for the phase current, which enables the motor to work at higher speeds compared to other type of converters.

The electrically isolated phase winding (between stator and rotor) of SR motor provides continuous operation even in fault conditions with decreased output power. Thus, SR motor can provide higher fault tolerance when compared with traditional DC and AC motors. However, SRMs are not free from fault, and therefore if it exists, it becomes critical

✉ E. Fantin Irudaya Raj
fantinirudhayaraj@drsacoe.com

[1] Department of Electrical and Electronics Engineering, Dr. Sivanthi Aditanar College of Engineering, Tiruchendur, India

[2] Department of Electrical and Electronics Engineering, SSN College of Engineering, Kalavakkam, India

in some reliability concerned applications where the productivity and cost should be minimized. Various diagnostic methods have been proposed by researchers to classify the electrical faults (open circuit fault and short circuit fault). The recent development in signal processing methods paved the way for different fault diagnosis methods.

Analysis of the literature in this article proceeded from the paper proposed by the authors in [1–3] where the authors have classified all the faults in SR motor and suggested some theoretical remedies. The solution for short circuit problem works only when the motor is at full load and operates at low speed. For the open circuit problem, the authors suggested us to operate the motor with an open diode. However, the proposed solutions are not effective when compared with the conventional method of disabling the affected phase approach. The authors of [4–7] investigated the automatic fault classification of SR motor using an HMM-based statistical approach. The modeling complexity of SR motors is decreased using the proposed method as it performs well in any operating mode. Also, the loading of the motor is not restricted to analyze the fault classification. The experimental study shows the superiority of the proposed method. This response time of the classifier is slow due to large set of training database.

Xiao et al. [8] made a qualitative analysis of the windings short circuit issue of SR motor. The authors have used FFT analysis to reconstruct the fundamental and harmonic frequency component of the winding current so as to obtain the positive and negative values of current. These current magnitudes are used to extract the fault features (short circuit fault) of SR motors. The effectiveness of this method against existing methods is verified using simulation and experimental setup. In [9–12], a compact model of the power converter for SR motor drive is introduced. The proposed bridgeless PFC converter integrates SR motor with a battery charger. Thus, bilinear functioning of the SR motor is realized. The FEA is used to analyze the current flowing through the windings. The mechanical losses arise because of swinging. The effectiveness of the proposed method is verified with simulation outcomes. Using [13–17] has improved the fault-tolerant capacity of the system using sensor-less square wave position edge identification for SR motor drives. The sensors are placed for all the poles of the rotor to enhance the fault detection in all the directions. A reliable fault classification is thus realized by integrating the inductance slope control approach with the proposed method to diagnose extreme failures. The computational complexity and hardware requirement are minimum. The simulated results are verified with the prototype model. In [18], the fastest fault diagnosis methodology to identify the faults in power converter transistors using the digital control method is proposed. The faults like over-current, voltage, and heating of transistors are measured to find the deterioration of power devices. This method uses two sensors to monitor the chopping, excitation, and freewheeling bus currents along with a single transistor. Still, this method could not perform well if the fault occurred on two transistors. It does not need any A/D converters, hence no delay in conversion, and therefore, the quick response is guaranteed. A novel approach is developed in [19] to detect the fault in the rotor position using a position sensor and two sensor-less methods. The position of the rotor is found at low and high speed using current chopping control and current gradient methods. An MLV (Maximum Likelihood Voting) algorithm is also utilized with the above methods to increase the reliability of SR motor drive. The high-reliability attribute makes them suitable for aerospace and automatic applications. Based on the above researches, a detailed survey of fault diagnosis and control methods of SR motor is conducted in [20]. With the simple mathematical modeling-based diagnosis method, the advantages, drawbacks, fault types, and their locations were compared with TE (Trial and Error) and digitizing methods. The digital methods are efficient in recognizing faults, but they cannot find the fault position. But TE methods are useful in finding the fault locations. The author also suggested future directions for enhancing the fault detection performance of SR motor drives.

The literature surveys [3, 21] show a lack of fault diagnosis and classification approaches that account for the performance degradation of SR motor. Most of the authors just described the behavior of SR motor under fault conditions without applying the diagnosis methods, which provides the precise classification results [22, 23]. As limited classification algorithms [24–26] are concerned with this issue in the literature, a statistical approach-based radial basis function (RBFNN) is proposed to mitigate the issue of the SR motor fault classifications.

The paper is structured into four parts. The proposed RBFNN fault classification method is discussed in Sect. 2. The results and discussion is given in Sect. 3, and the conclusion is presented in Sect. 4.

2 Proposed RBFNN Based Fault Classification Method

The complete schematic of the proposed method is given in Fig. 1. The input ac power is rectified using diode bridge rectifier. Then, the rectified dc power is stored in a capacitor bank. A unipolar switching sequence is provided by BR converter where two switches (n + 1) and two diodes (n + 1) are placed in each phase (n) with independent controls. So as to have a quick building up of excitation current, a higher switching voltage is needed. Also, the rotor position and current excitation must be synchronized to get ripple-free torque output. The upper switches of the converter perform switching action while the lower switches provide commutation. The optical encoder is used to sense the position and

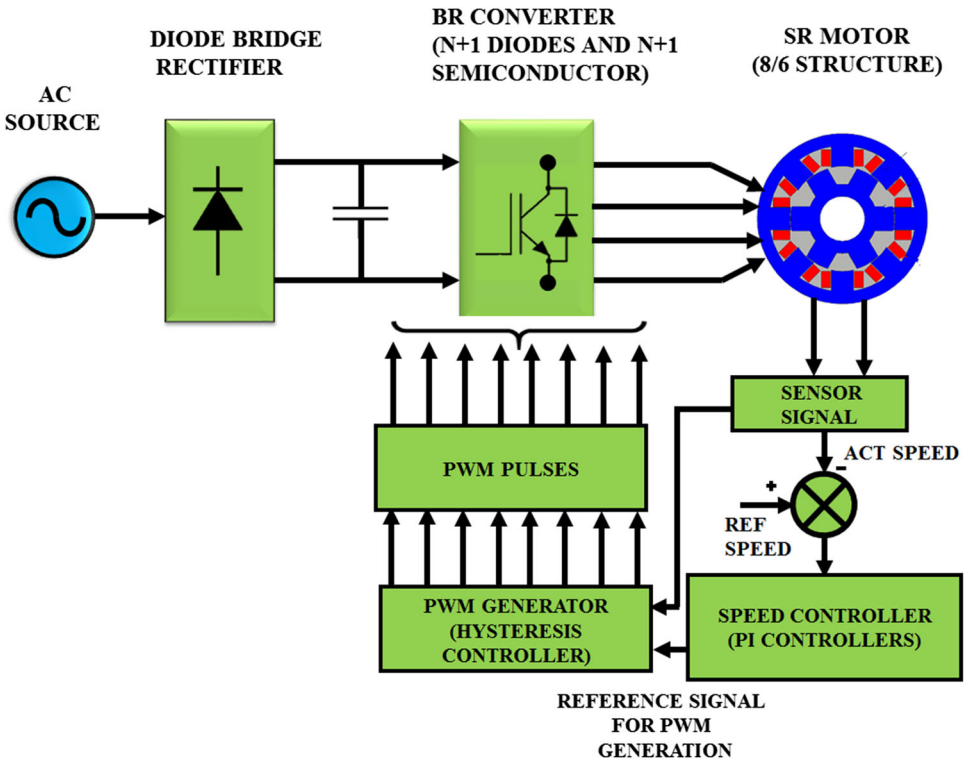

Fig. 1 Block diagram of SR motor drive

speed of rotor. PI controller compares this speed with the reference speed. The output of PI controller is the reference phase current of SR motor. The hysteresis controller generates the PWM pulses of the converter by comparing the reference phase current and actual current. The optimization techniques such as cuckoo search algorithm (CSA), incremental attribute learning optimization algorithm (IALOA), and Monte Carlo simulated combined particle swarm optimization (MCSPSO) are used for tuning the parameters of PI controller.

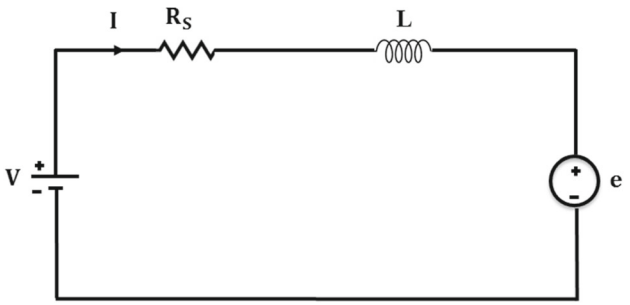

Fig. 2 Electrical equivalent circuit of SR motor phase

2.1 Modeling of SR Motor

2.1.1 Electrical Equivalent Circuit

The electrical equivalent circuit of a phase of SR motor shown in Fig. 2 consists of resistive and inductive impedances. The influence of magnetic saturation, flux linkage, leakage flux, and the mutual inductive coupling of phases is assumed to be negligible so as to design a simple mathematical model. The linear model of the SR motor is described by three differential equations, such as voltage equation, the motion equation, and the EM torque equation.

2.1.2 Mathematical Equations

In SR motor, the electromagnetic torque is generated by utilizing the rotor position-based magnetic reluctance linked with every phase. When a particular phase is excited, the torque is generated by which the rotor gets aligned with the stator. The dynamic model of the SR motor consists of a set of mathematical equations.

The per phase voltage equation is expressed as

$$V = R_s i + \frac{\mathrm{d}\lambda(\theta, i)}{\mathrm{d}t} \tag{1}$$

where R_s is the resistance of a phase and λ is the flux linked with a phase and it is related to inductance as

$$\lambda = L(\theta, i)i \tag{2}$$

where L is the inductance per phase whose magnitude depends on the position of the rotor and current in a phase.

On substituting Eq. (2) in Eq. (1), the per phase voltage equation becomes

$$V = R_s i + L(\theta, i)\frac{\mathrm{d}i}{\mathrm{d}t} + \frac{\mathrm{d}L(\theta, i)}{\mathrm{d}\theta} i\omega_m \tag{3}$$

where ω_m is angular velocity. The induced EMF is expressed as

$$e = \frac{\mathrm{d}L(\theta, i)}{\mathrm{d}\theta} i\omega_m = i\omega_m k_b \tag{4}$$

where k_b is an EMF constant and is derived as

$$k_b = \frac{\mathrm{d}L(\theta, i)}{\mathrm{d}\theta} \tag{5}$$

The torque per phase is given by

$$T_e(\theta, i) = \frac{1}{2} i^2 \frac{\mathrm{d}L(\theta, i)}{\mathrm{d}\theta} \tag{6}$$

Assuming the motion of the magnetic field to be linear, the torque equation is now expressed as

$$T_{\text{total}}(\theta, i) = \sum_{\text{phases}} \frac{1}{2} i^2 \frac{\mathrm{d}L(\theta, i)}{\mathrm{d}\theta} \tag{7}$$

the equivalent mechanical torque equation is

$$T_{\text{total}} - T_l = J_m \frac{\mathrm{d}_{\omega_m}}{\mathrm{d}t} + B_m \omega_m \tag{8}$$

where T_l is load torque, J_m is inertia moment, and B_m is the frictional coefficient.

The expression for average torque is given by

$$T_{\text{average}} = \frac{1}{T} \int_0^T T_{\text{total}} \tag{9}$$

Torque ripple is measured as

$$T_{\text{ripple}} = \frac{T_{\text{total (calculated)}} - T_{\text{total (measured)}}}{T_{\text{average}}} * 100\% \tag{10}$$

2.2 BR Converter for SR Motor Drive

In SR motor drives with BR converter, the phase windings are in series with the switches of every phase. When a shoot-through fault occurs, the winding inductance suppresses the rising rate of current and gives enough time to start isolated protection against the faults. The winding failure in a particular phase does not affect other phases as the phases of SR motor are independent of each other. Thus, an uninterrupted functioning of the motor is guaranteed with decreased output power.

2.2.1 Circuit Diagram of BR Converter

The most commonly used converter in SR motor is the asymmetric bridge converter. The phases of SR motor are individually associated with the half-bridges (consisting of two switches and two diodes) of asymmetric converter. The circuit of the asymmetric bridge converter for an 8/6 SR motor is illustrated in Fig. 3.

The total DC voltage is utilized for energizing and de-energizing the phases during the hard-chopping stage. When a switching pair is turned on, the winding phase gets energy from the DC supply. When both the switches are switched off, the commutation current flows to the diode from the switch, now the voltage across the phase will be at a negative potential. These asymmetric half-bridges allow soft switching to obtain a zero-voltage freewheeling condition; thus, the phase is excited from the positive potential and commutated at zero potential. There is no boundary present to stop exciting the two phases at the same instant to achieve high torque. The drawback of this converter is the increased number of power electronic components in every half-bridge (two switching devices and diodes).

2.3 PI Controller

In a closed loop system, a PI controller receives an error signal to vary the controlling parameter and achieves the required response from the system. The controlling variable may be speed, torque, and flux or any measurable quantity. The advantage of the PI controller is from the empirical adjustment of one or more gain esteems; the change in response of the system can be observed [9]. It is necessary to use PI controller more frequently so as to get the proper control of the system. The blunder signal is produced by comparing the desired and measured value of the parameter. The polarity of the error gives the directional change in the input and results in a small steady-state error. The integration (I) term minimizes these steady-state errors. The 'I' term indicates the time required to run the controller. These steady-state errors are accumulated into a large value with respect to time. The obtained error signal is multiplied by 'I' factor.

2.3.1 PI Controller Tuning

A PI controller is introduced in process control firms. Various functions using PI controller are realized to achieve specific performance indices of system [13]. Usually, tuning is done to determine the controller constants, and it depends on the dynamics of the system. The basic block is shown below to exhibit various tuning techniques where the blunder among the expected and the measured yield is the controller input.

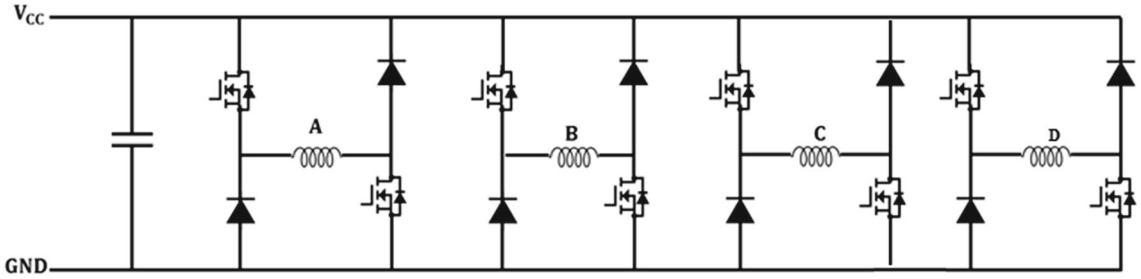

Fig. 3 Asymmetric bridge converter

This error is processed to produce the required command signal for the system and is expressed as,

$$U(s) = K_{\mathrm{p}}(1 + 1/\tau_i) \tag{11}$$

$$\text{or in time domain } U(t) = K_{\mathrm{p}}[e(t) + (1/\tau_i)\int e\mathrm{d}t] \tag{12}$$

where Kp, proportional gain; τ_i, integral time constant.

The optimization techniques such as cuckoo search algorithm (CSA), incremental attribute learning optimization algorithm (IALOA), and Monte Carlo simulated combined particle swarm optimization (MCSPSO) are used for tuning the parameters of PI controller.

2.4 Fault Classification Using RBFNN

Our proposed system shown in Fig. 4 focuses on the area of the fault and to detect the types of faults by making use of speed-based fault analysis. This paper describes an application of DCT-based DOST transform with an adaptive threshold for fault determination by making use of recorded signals from the trained dataset. A Gabor filter filters the noisy distortion which is existing in the speed waveform. It helps to preserve the information of speed waveform. After removing the noise, the signal gets partitioned into its constituent parts (i.e., 256 samples), and the amplitude is computed to analogize with trained data. It is computed to detect the types of fault. Variations in the amplitude and duration of the speed sample help for the analysis of fault. A total of 1000 samples were taken for analysis. The sampling frequency is 100 hertz, and it is split up into five intervals to detect the fault. In feature extraction, the mean and average value is evaluated. A genetic algorithm is implemented for extracting the feature. Currently, there has been a boom in applying hereditary calculations for minimizing the multi-target enhancement issue. In a vast arrangement space and high advancement execution, it offers considerable preferences in these types of faults in the SR motor. In this algorithm, among the available classes, an appropriate margin was selected, and then, highlights are labeled depending on the class combined with a specific class. The significant one that needed to be done is the features that are extracted must be screened clearly to avoid the issue of redundancy and irrelevancy. By applying this algorithm, the faults were found out, and the segment length (mean value of fault waveform cycle) and the average have been identified, and finally, RBFNN classifier is used for analogizing with the trained data. The classifier network is trained with motor speed under different fault occurrence and normal conditions. As the classifier is enabled with artificial intelligence, the system detects the types of a fault occurring the SR motor. The analogy is performed in the ratio 1:6. The output of the proposed work is evaluated quantitatively and qualitatively for testing the performance of the algorithm. The accuracy achieved in this proposed work is 98.5%. While analogizing with existing works, it achieves the best result and high accuracy.

2.4.1 Preprocessing

Preprocessing of speed signal is the first and foremost step to be performed for the enhancement of the image data that suppresses the noisy distortions or enhances the feature of the image for post-processing. The number of specimens taken for analysis has been elaborated to 1000 samples.

2.4.2 GABOR Filter

It is a type of linear filter whose impulse response is characterized as a coherence function combined with a Gaussian function. The response of Gabor filter is working well in techniques such as texture segmentation and iris pattern recognition. The significance of using this filter in our proposed work is as per the uncertainty principle, and they persuade the minimum space bandwidth product. Gabor filter was implemented for signal representation in terms of both time and recurrence from the SR motor speed signal. The unpredictable theory to describe the product of the propagation of a signal in the time and recurrence domain must exceed or equals the fixed constant.

$$\Delta t \Delta f = c \tag{13}$$

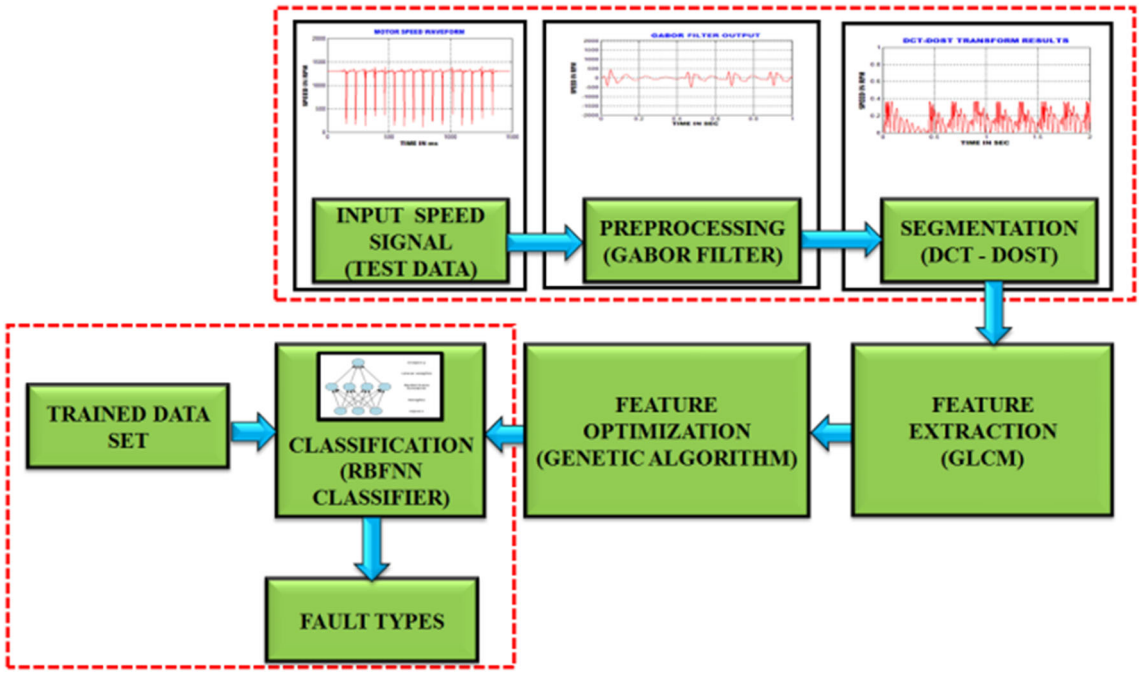

Fig. 4 SR motor speed-based fault analysis block diagram

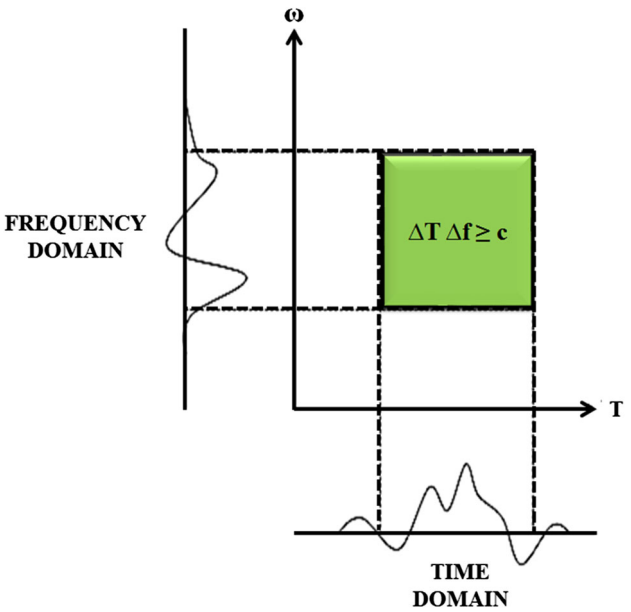

Fig. 5 Time and frequency domain

where c is a constant, Δt and Δf is the measure of the time and recurrence space.

In 2D form shown in Fig. 5, the variable of time t, is superseded by (x, y) coordinates in the spatial space and the variables of frequency f are superseded by variable (u, v) in the recurrence space. 2D Gabor filters are widely utilized in most of the picture processing techniques to extract features and speed analysis. The 2D Gabor function is evaluated as,

$$g(x, y) = \frac{1}{2\pi\sigma_g^2} e\left[\frac{-x^2 + y^2}{2\sigma_g^2}\right] \exp(j2\pi f(x\cos\theta + y\sin\theta)) \tag{14}$$

In the frequency domain,

$$g(u, v) = e\left\{-\frac{1}{2}\left[\frac{(u-w)^2}{\sigma_u^2} + \frac{v^2}{\sigma_v^2}\right]\right\} \tag{15}$$

where $\sigma u = \frac{1}{2\pi\sigma x}$ and $\sigma v = \frac{1}{2\pi\sigma y}$,

while σx and σy are the standard deviation of the elliptical Gaussian in the x-axis and y-axis. The DC esteems of two-dimensional Gabor filter were taken to suppress the higher-order reaction for exact amplitude esteems. The filter parameter is computed by using the formulas,

$$a = \left(\frac{u_h}{u_l}\right)^{-\frac{1}{s-1}} \tag{16}$$

$$U_{O=\frac{U_n}{a(s-m)}} \tag{17}$$

and σ_u is computed by using the equation,

$$\sigma_{u=\frac{(a-1)U_0}{(a+1)\sqrt{2ln2}}} \tag{18}$$

σ_v evaluated by using,

$$\sigma_v = \tan\left(\frac{\pi}{2k}\right)\left[U_n - 2\ln\left[\frac{\sigma_{u^2}}{U_h}\right]\right]\left[2\ln 2 - \frac{(2\ln 2)^2\sigma_u^2}{U_h^2}\right]^{\frac{1}{2}} \quad (19)$$

where S represents the overall number of stages and the value of m ranges from 0, 1, …, $S-1$, and σ_u and σ_v are the standard deviation of the elliptical Gaussian in the frequency domain.

By applying the Gabor filter on the binary image, the computation becomes too simple, and it generates a perfect improved result. Comparing with simple filters, multi-resolution filters are time-consuming.

2.4.3 Segmentation

The segmentation procedure partitions the input image into constituent parts or objects. In digital image processing, it is a challenging task in autonomous segmentation. A cragged segmentation procedure brings the process a long way toward the best solution of imaging problems that require an object to be detected individually. In this proposed work, segmentation is performed by using DCT-based DOST. It helps to partition an image into 256 samples.

2.4.4 DCT Based DOST

To effectively portray the speed signal in time-recurrence space, discrete cosine-based DOST is applied. Furthermore, the data are registered and linked to the morphological list of capabilities to comprise the last best highlights set, which is used for classification by using RBFNN. In the past decades, they used FT, STFT, etc. These transforms faced a problem of selecting the wavelet and the sampling frequency. It leads to misleading information. To conquer the restriction of generally utilized old style signal preparing methods like FT, STFT, and WT, a novel methodology is introduced in this study. This methodology utilizes the DCT-DOST scheme. It examines the time-recurrence dissemination of the speed signal and distinguishes the fault naturally. In DOST, the source sign is mentioned occasionally in DFT. During coefficients truncation, the sign will, in general, lose its structure in the event of DOST. However, with DCT, it withstands more during truncation of coefficients. DCT is genuinely esteemed, and it does exclude any negative recurrences to limit the unpredictability. The benefits of DCT in DOST combines the vitality and indicates the important coefficients at the lower recurrences.

DOST transformation:

The S transform is said to be linear to build the space between FT and wavelet. The S transfer for any info sign $h(t)$ is given by,

$$s(\tau, f) = \frac{|f|}{2\pi}\int_{\alpha}^{-\alpha} h(t)e^{-\frac{(t-t)^2 f^2}{2}} e^{-i2\pi f t}\mathrm{d}t \quad (20)$$

Width of the window is indicated as,

$$\sigma(f) = T = \frac{1}{|f|} \quad (21)$$

$\delta(\tau, f_0)$ shows the 1-D time function for a fixed recurrence f_0, and it shows how the amplitude and frequency change over time. The DOST of h(KT) is expressed as,

$$H\left[jT, \frac{n}{NT}\right] = \sum_{m=0}^{N-1} H\left[\frac{m+n}{NT}\right]G(m,n)e^{\frac{i2\pi mj}{N}} \quad (22)$$

where

$$G(m,n) = e^{-\frac{2\pi^2 m^2 n^2}{n^2}}$$

where n ranges from 1, 2, …, $N-1$.

It contains only positive frequencies, and it takes no symmetry in the coefficients. As an outcome, to adjust a frequency space while partitioning, higher frequencies are required. Since the DCT-DOST contains no negative frequency, the width of the frequency for any info signal of length 2^N is indicated as below,

$N_i = 1$ for $i < 2$

$N_i = 2^{i-2}$ for $2 \le i \le N-1$

The proposed algorithm for DCT-DOST is as follows,

$Y = dct(y)$;

$z = 0$

$Forcyin[1, 2, 3, \ldots]$;

$Y[z; z+(z-1)]; idct(y[z; z+cz-1])$;

end

return y

The architecture of the DCT-DOST segmentation is shown in Fig. 6.

The reverse DCT is computed as follows,

$$x(n) = \sqrt{\frac{1}{N}X(0) + \sqrt{\frac{2}{N}}\sum_{k=1}^{N-1} x(k)\cos\left(\frac{\pi(2n+1)k}{2N}\right)} \quad (22)$$

where n ranges from 0, 1, … $N-1$.

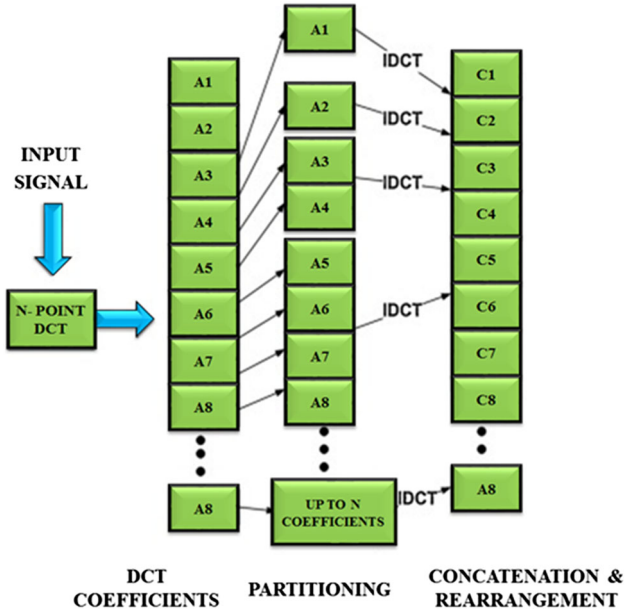

Fig. 6 DCT-DOST ARCHITECTURE

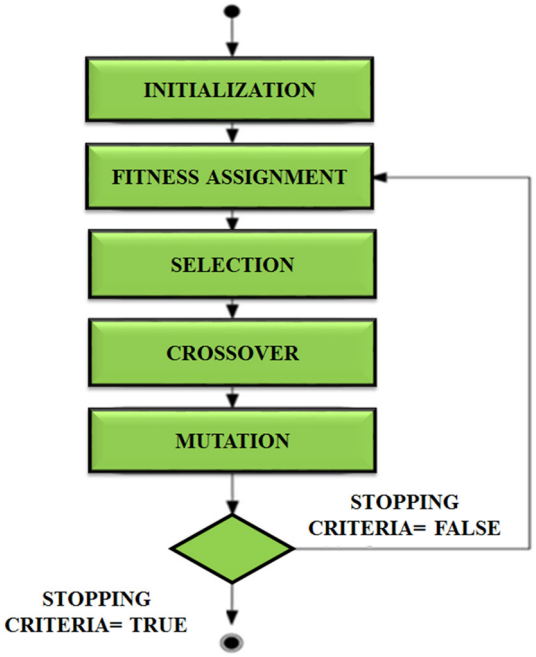

Fig. 7 Structure of the genetic algorithm

β denotes the length of the recurrence range, t indicates the time parameter, and v_i is the frequency variable.

To ensure orthogonality, some conditions needed to be followed,

(1) $t = 1, 2, \ldots \beta - 1$

Selection of width of the frequency band β and frequency variable V_{i} which is to be used only once.

These awry time-recurrence coefficients are determined for all the speed signals which are used for additional examination.

2.5 Feature Extraction

The morphological highlights which were taken contain maximum and minimum points of each sample of the signal. It is estimated by using the equation,

$$f(t) = f(t) - \frac{\min(t)}{\max(t)} - \min(t) \tag{23}$$

The next phase is to reduce the feature. To perform this operation, a genetic algorithm is applied. The features which were taken were fed into the four different neural networks for training, and then, it is tested by applying various test files. For each neural network, accuracy is computed.

The next phase needed to be performed is feature reduction. It is performed by using genetic algorithm shown in Fig. 7. Recently, there has been a boom in applying a genetic algorithm for minimizing the enhancement issues. In highly complicated execution and in a massive set of arrangements, this algorithm is applied. It was used to optimize the features and neural network for Speed signal identification. It helps to extract the best features, and it is included in the next generation. The next generation picks out favorable conditions, and the rest will be omitted. It initially repeats and develops a population by generating a new population at each step by the process of

(1) Selection,
(2) Crossover and
(3) Mutation.

And finally, it applies a fitness function; fitness value is computed by using the equation,

$$f.f = \frac{1}{n}\sum_{i=1}^{n}(t - \mathrm{out}) \tag{24}$$

N represents the number of outputs, and t indicates the target output, and out denotes the actual output. The fitness function which was taken may contain positive and negative values. So we cannot make use of fitness value directly. The working of three operators is as follows. The selection operator is applied to figure out the best features which are present with the best fitness score and transfer it to the next generation. To generate the offspring chromosome, the crossover

operator performs swapping between the selected individuals.

$$\text{Chromosome } i \text{ reproduce} = \frac{f(xi)}{\sum_{k=0}^{1} f(xk)} \tag{25}$$

Then, the final operator is applied to alert the bit, which is in the chromosome. The probability is computed that chromosome in the nth place will be evaluated by using,

$$P_n = \frac{N - N + 1}{\sum_{i=1}^{N} i} \tag{26}$$

This algorithm helps in optimizing the outcome of the neural network, and it performs well to get a good prediction accuracy, sensitivity, and specificity. It gives its output for better classification. The RBFNN classifier is used for better classification performance.

2.6 RBFNN Classifier

It is a special class of function involved in predicting the time series, classification, and function approximation. It can be applied to any sort of models such as linear and nonlinear and in any network. The three layers of RBFNN shown in Fig. 8 are the input layer, hidden layer, and output layer. The hidden layer provides a nonlinear conversion of the input to the hidden layer. The output layer combines in a linear way the activation of the hidden layer. The input layer can be modeled as a vector of actual numbers $x \epsilon R^n$. The outcome of the network: $R^n \rightarrow R$, given by,

$$\varphi(x) = \sum_{i=1}^{N} a_i x(||x - c_i||) \tag{27}$$

where N represents the neurons quantity, which is present in the hidden layer, C_i denotes the center vector, and a_i indicates the weight of the neuron. The parameters a_i, c_i and β_i help to optimize the fit between φ and the data.

The first layer involved is the input layer. A typical radial function of the scalar input vector is expressed as,

$$h(x) = e\left(-\frac{(x-c)^2}{r^2}\right) \tag{28}$$

The generated input may be normalized and in de-normalized form. If it is found in a de-normalized state. It is computed by using the equation,

$$\varphi(x) = \frac{\sum_{i=1}^{N} a_i \rho(||x - c_i||)}{\sum_{i=1}^{N} \rho(||x - c_i||)} \tag{29}$$

where

$$u(||x - c_i||) = \frac{\rho(||x - c_i||)}{\sum_{j=1}^{N} \rho\left(\left|\left|x - c_j\right|\right|\right)}$$

It is known as the normalized basis function. In the normalized and de-normalized case, higher-order linear terms are also possible.

This result can be written as,

$$\varphi(x) = \sum_{i=1}^{2N} \sum_{j=1}^{n} e_{ij} v_{ij}(x - c_i) \tag{30}$$

where

$$e_{ij} = \begin{cases} a_i, & \text{if } i \in [1, N] \\ b_{ij}, & \text{if } i \in [N+1, 2N] \end{cases} \quad \text{and}$$

$$v_{ij}(x - c_i) = \begin{cases} \delta_{ij}\rho(||x - c_i||), & \text{if } i \in [1, N] \\ \left(x_{ij} - c_{ij}\right)\rho(||x - c_i||), & \text{if } \in [N+1, 2N] \end{cases}$$

In the de-normalized case and

$$v_{ij}(x - c_i) = \begin{cases} \delta_{ij} u(||x - c_i||) & \text{if } i \in [1, N] \\ \left(x_{ij} - c_{ij}\right)u(||x - c_i||) & \text{if } \in [N+1, 2N] \end{cases}$$

In the normalized case

$$\delta_{ij} = \begin{cases} 1, & \text{if } i = j \\ 0, & \text{if } i \neq j \end{cases}$$

The probability density function is computed between the input and the output space by using,

$$p(x) = \int p(x \Lambda y)\mathrm{d}y = \frac{1}{N} \sum_{i=1}^{N} \rho(||x - c_i||) \tag{31}$$

The expectation of y given an input x is

$$\varphi(x) = E(y|x) = \int y P(y|x)\mathrm{d}y \tag{32}$$

where

$P\ (y|x)$ is the conditional probability of y given x.

RBFNN is especially used for classification. For performing classification, trained and test set data are needed. The data are retrieved from a trained database. It contains both normal and pathological dataset. Nearly 60% of data have been taken for training, and the rest 40% was taken for testing. The training set in which there are n pairs. It is represented in the form of

$$T = \{(x_i, y_i)\}_{i=1}^{p} \tag{33}$$

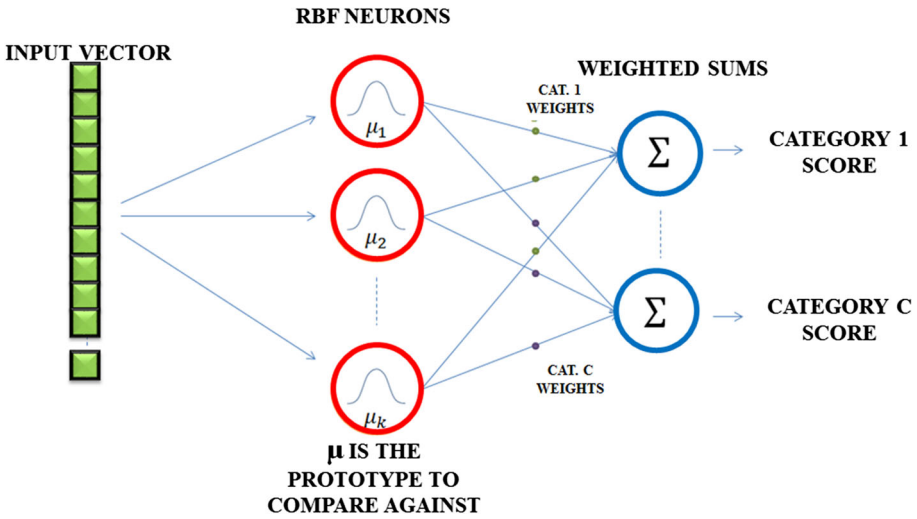

Fig. 8 RBFNN network

Y_i indicates the output value of a trained set and then time prediction is concerned about estimating the next esteem and features of a sequence such as

$$\ldots, y_t - 3, y_t - 2, y_t - 1, \ldots$$

Time prediction is difficult when compared to straight regression or classification. RBFNN classifier works well in classification, and to obtain the answer of actual multivariable interpolation issue, a radial basis function was introduced. An unpredictable sample grouping issue cast in a high dimensional space nonlinearly is bound to be straightly distinct than in a low-dimensional space. This leads to consider the multivariable interpolation problem in high-dimensional space. It helps in achieving all these problems and the accuracy (acc) is measured by using,

$$\text{acc} = \frac{\text{TP} + \text{TN}}{\text{TP} + \text{TN} + \text{FP} + \text{FN}} \times 100\% \tag{34}$$

Sensitivity is measured by using,

$$\text{Se} = \frac{\text{TP}}{\text{TP} + \text{TN}} \times 100\% \tag{35}$$

Specificity is measured by,

$$\text{Sp} = \frac{\text{TN}}{\text{TP} + \text{TN}} \times 100\% \tag{36}$$

where TP, TN, FP, and FN indicate the true positive, true negative, false positive, and false-negative. N_T indicates the number of correctly classified speed signal. It achieved a high accuracy of 98.75% obtained by RBFNN filter.

3 Results and Discussion

3.1 Normal Condition (Before Faults)

The SR motor is simulated at normal and fault conditions. Initially, the SR motor is operated at a healthy state, and the corresponding current, torque variation, speed, and flux are measured. Then with the OC and SC faults, the same parameters are obtained for the different phases.

The following responses shown in Fig. 9 are plotted between flux (Wb) and time (s) for the parameter flux determination and current (A) and time (s) for the parameter current determination and torque (N-m) and time (s) for the parameter torque determination.

The response of motor speed and current for the same torque–speed characteristics of 10 Nm-1500 rpm shown in Fig. 10 has the effect of torque ripple on the speed because of the low inertia of the motor.

DC supply voltage and current are 220 V and 5.4 A. The Rotor position sensor is placed on the motor shaft. The turn-on and turn-off angles of the converter are maintained fixed at 30° and 45°. The switching angles can be used to control the produced torque. Torque ripple is estimated using Eq. (10), and the resultant torque ripple is 0.282.

3.2 1 Open Circuit Faults

The response of flux, current, and torque of SR motor under 1Φ open circuit fault for different optimization and PI controllers are shown in Figs. 11, 12 and 13. In 1Φ open circuit fault, phase A is open circuited in the time interval 0.1 s to 0.2 s. Hence, current will not flow in phase A alone. It is noticed that the values of $T_{\max}$, $T_{\min}$, and mean torque are 7.68 Nm at a load of 3 Nm. The torque ripple is estimated using Eq. (10), and the obtained torque ripple is 0.508.

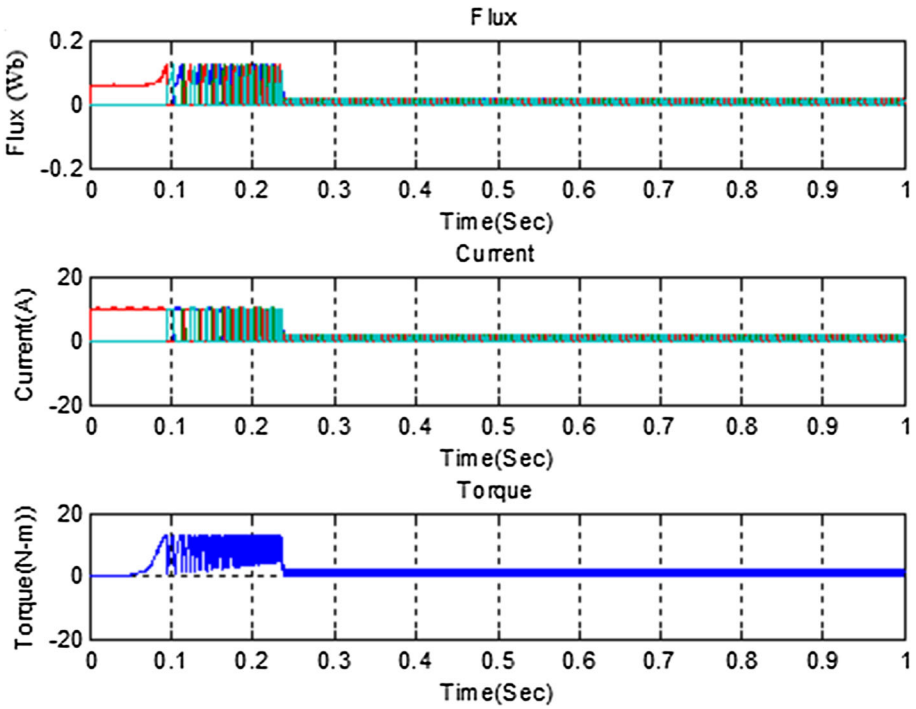

Fig. 9 Normal condition (before faults)

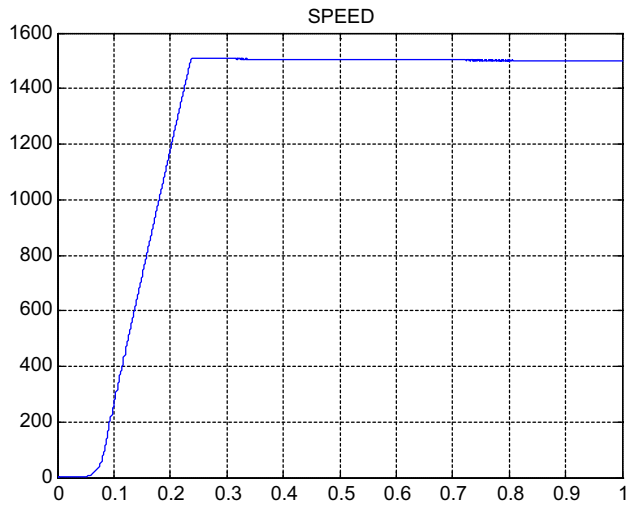

Fig. 10 Speed response in normal condition (before faults)

3.3 1 Short Circuit Faults

The response of flux, current, and torque of SR motor under 1Φ short circuit fault for different optimization and PI controllers are shown in Figs. 14, 15 and 16. Now phase B is short-circuited, and hence, the number of turns on this phase is decreased. With this reduction, the mean torque of this phase is also reduced. The values of T_{max}, T_{min} are observed and the mean torque is 6.23 Nm at a loading of 3 Nm, and the obtained torque ripple is 0.569.

3.4 Open Circuit Fault in Two Phases

The response of flux, current, and torque of SR motor under double-phase open circuit fault for different optimization and PI controllers are shown in Figs. 17, 18 and 19. The open circuit fault occurred in any two phases at the time of 0.1 s to 0.2 s for phase A and 0.15 s to 0.24 s for phase B. So, the current will not flow in phase A and phase B. The values of T_{max} and T_{min} are observed and mean torque is 7.15 Nm at a loading of 3 Nm. The torque ripple is 0.412.

3.5 Short Circuit Fault AT Double Phase

The response of flux, current, and torque of SR motor under double-phase short circuit fault for different optimization and PI controllers are shown in Figs. 20, 21, and 22. The values of T_{max} and T_{min} are observed, and the mean torque is 6.75 Nm at a loading of 3 Nm. The obtained torque ripple is 1.230.

The speed control with torque ripple reduction of SR motor is proposed in this paper. The PI controller is used to control speed and the current. The performance parameters are obtained from simulation for improving the SR motor drive. Speed response of various optimization is used in this paper. The optimization techniques are CSA, IALOA, MCSPSO (Tables 1, 2, 3, 4 shows the rise time (T_r), peak time (T_p), Settling time (T_s) and steady-state error (E_{ss})).

At the time of fault condition, the speed response of SR motor with conventional PI controller and by using various optimization-based tuned PI controllers is shown in Figs. 23, 24, 25 and 26. The motor is working at the estimated speed

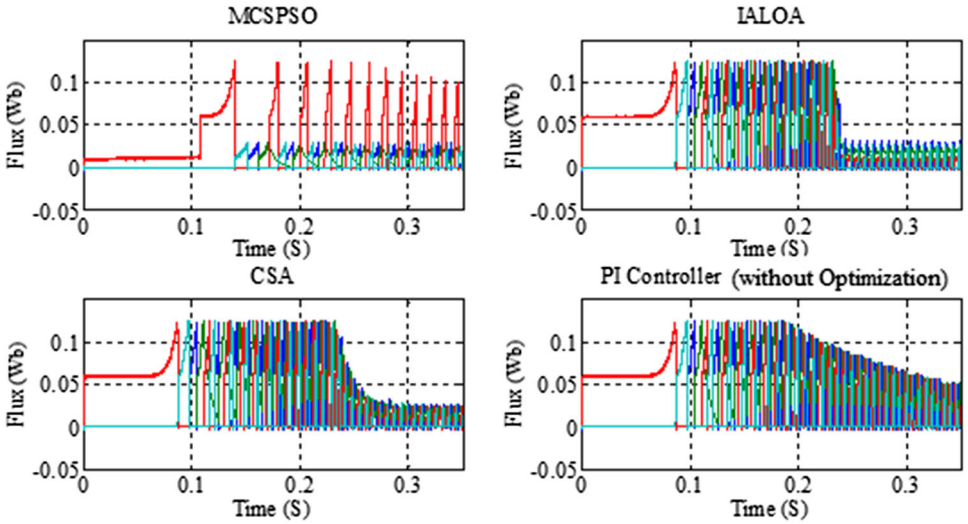

Fig. 11 Flux linkage versus time characteristics

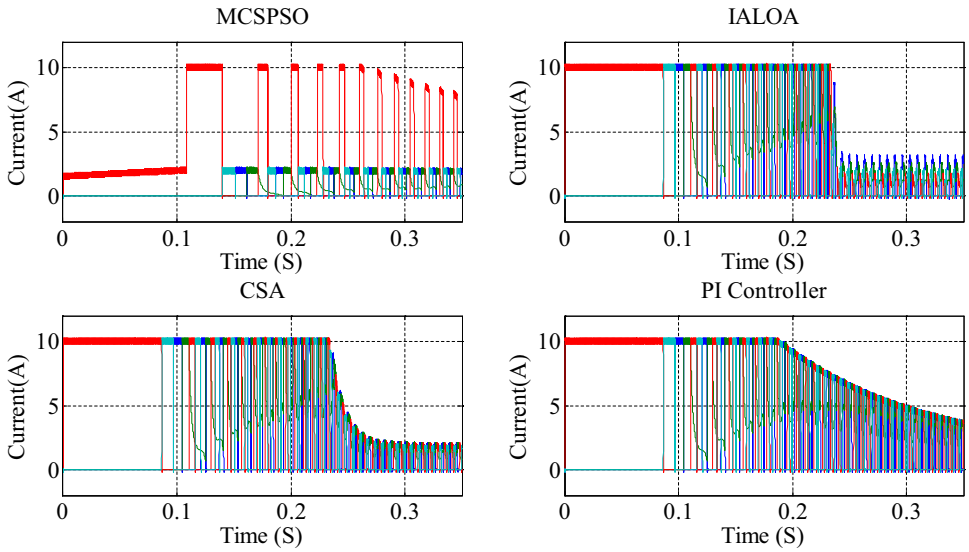

Fig. 12 Current versus time characteristics

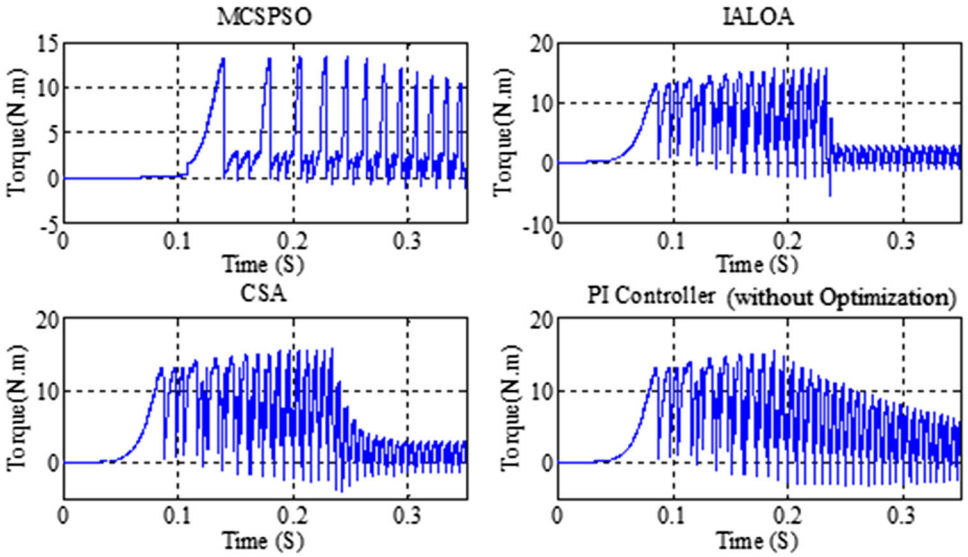

Fig. 13 Torque versus time characteristics

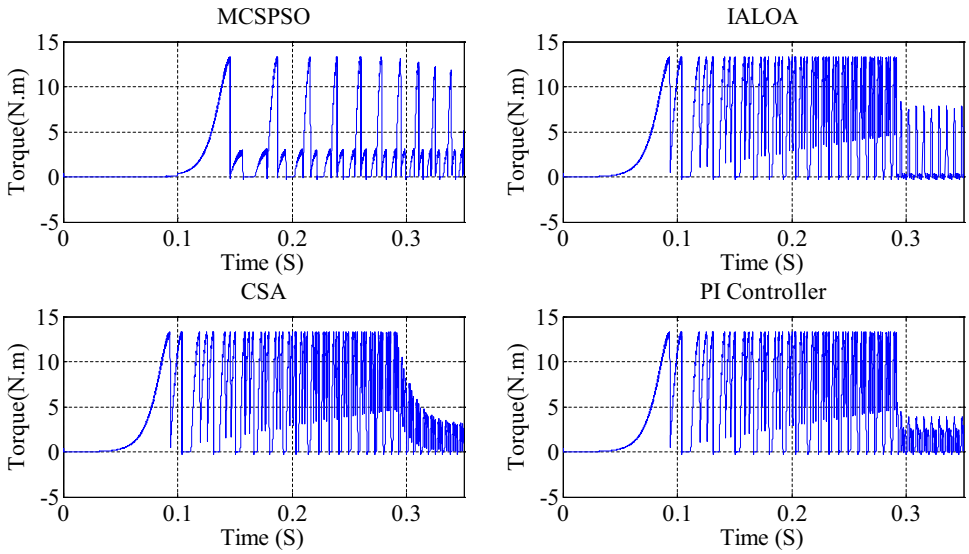

Fig. 14 Flux linkage versus time characteristics

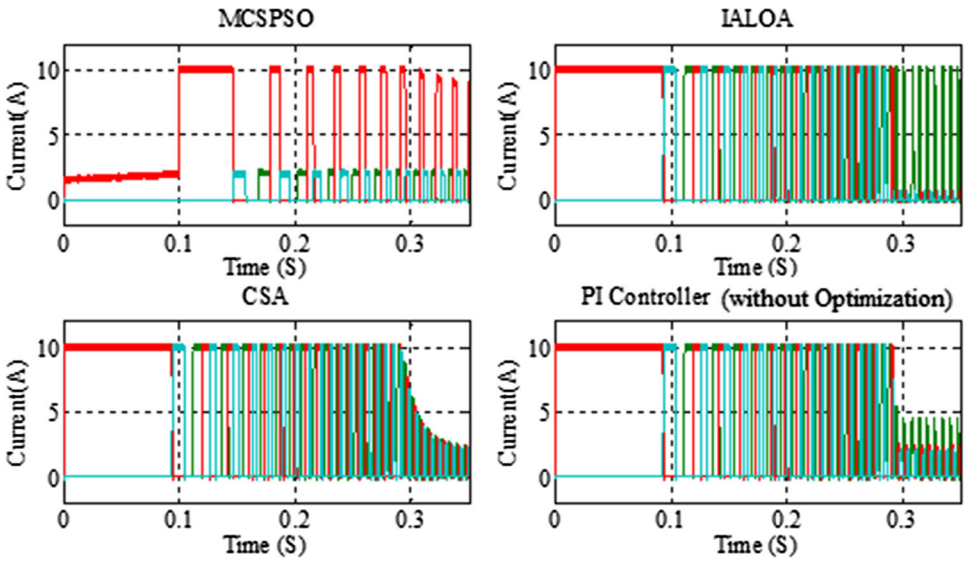

Fig. 15 Current versus time characteristics

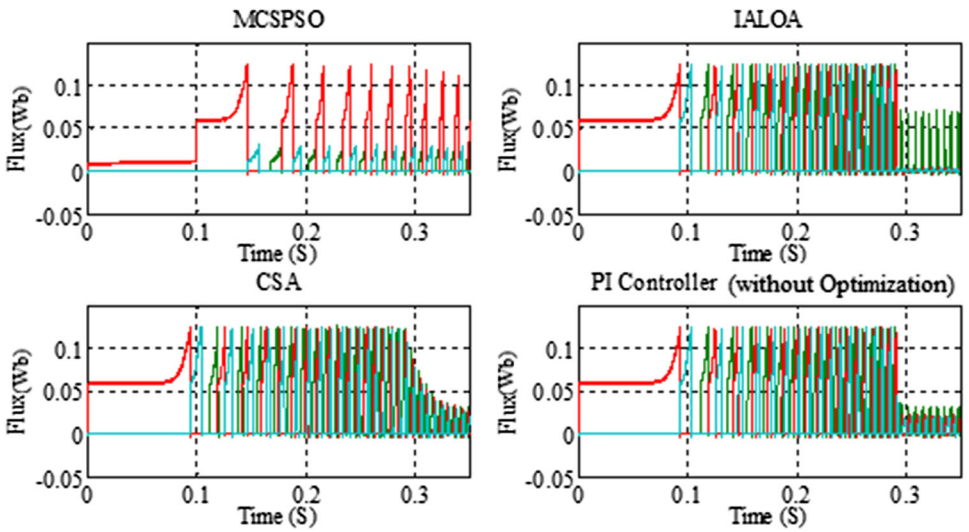

Fig. 16 Torque versus time characteristics

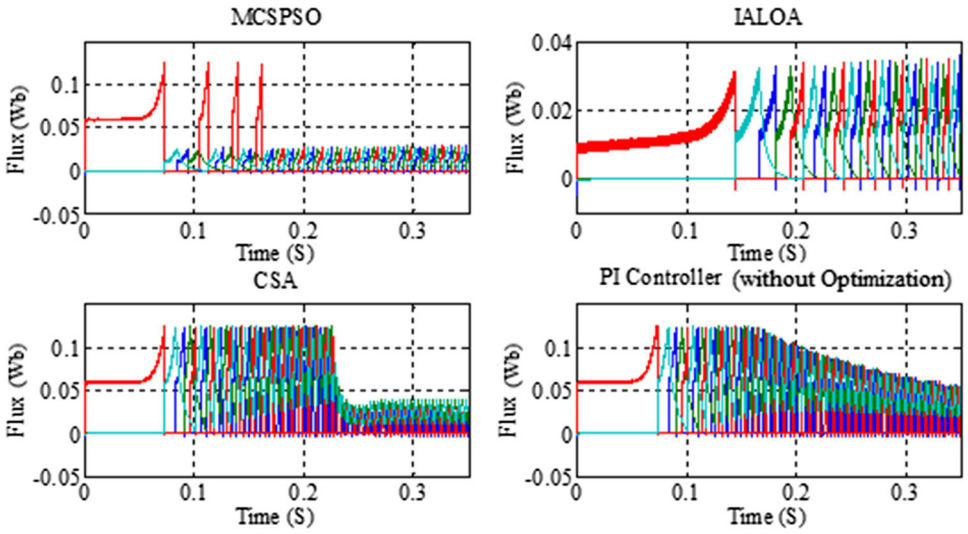

Fig. 17 Flux linkage versus time characteristics

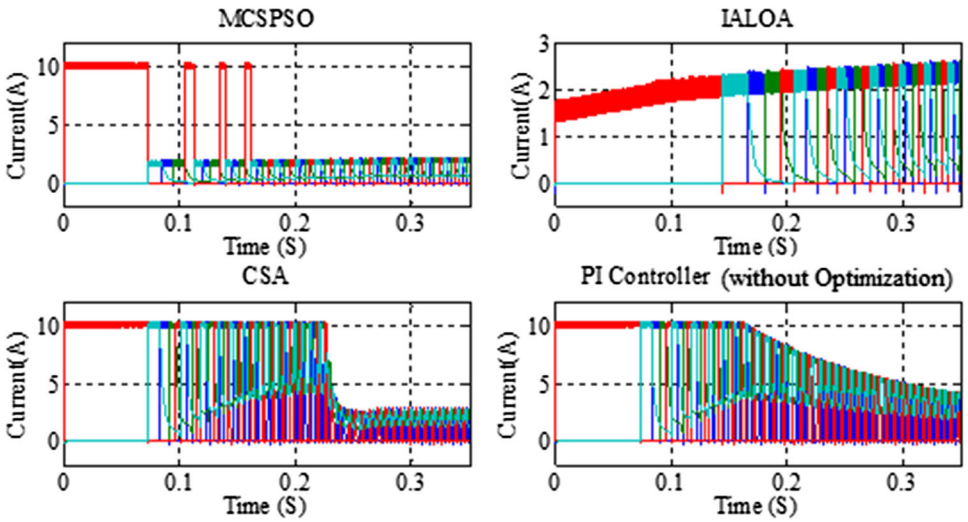

Fig. 18 Current versus time characteristics

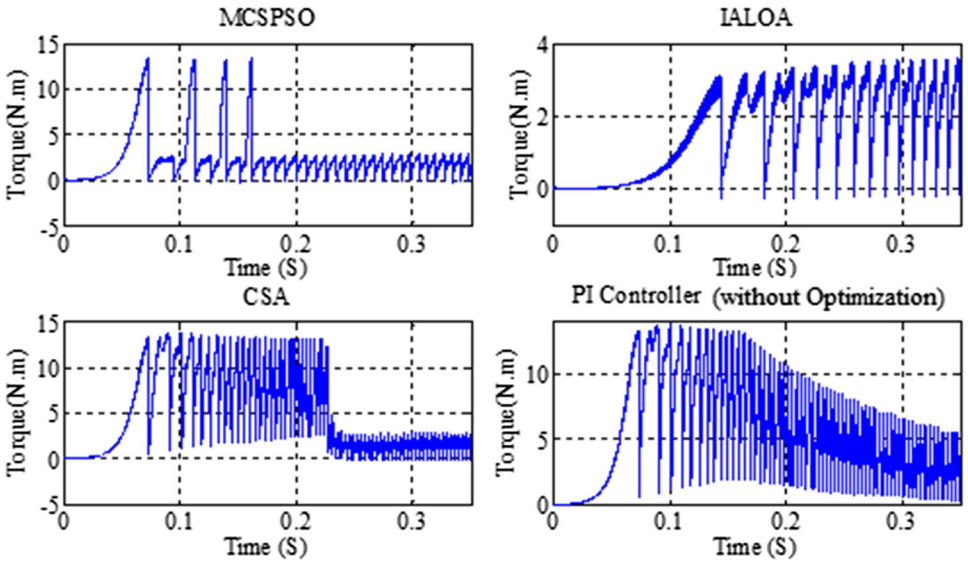

Fig. 19 Torque versus time characteristics

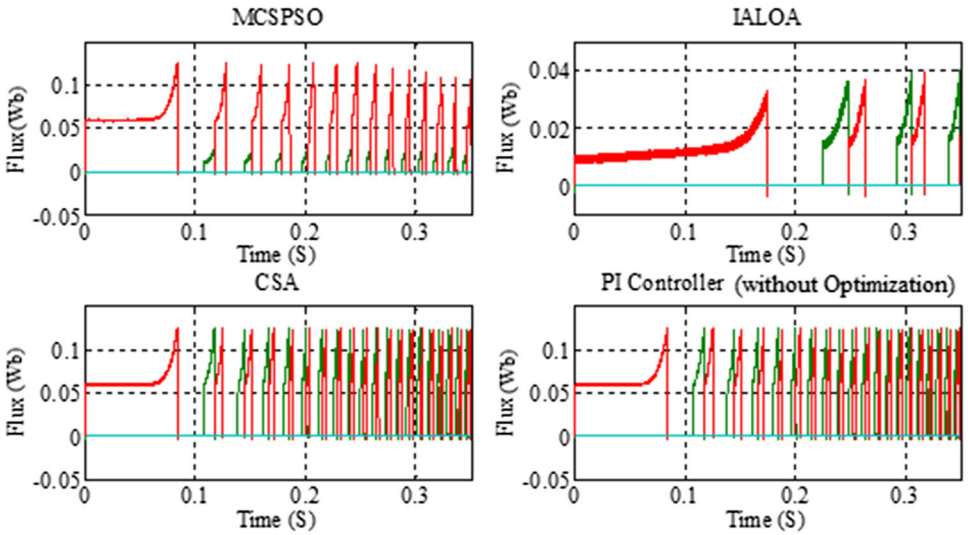

Fig. 20 Flux linkage versus time characteristics

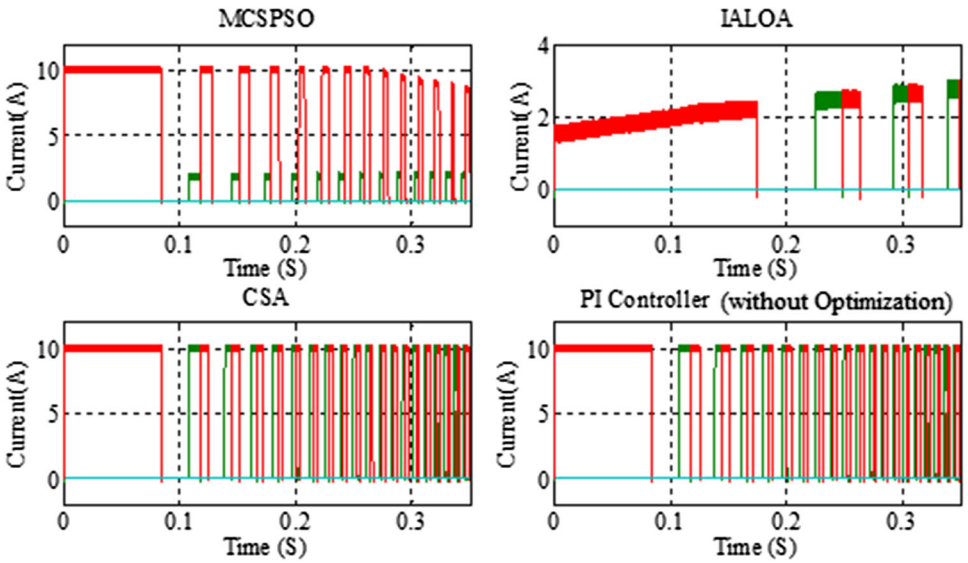

Fig. 21 Current versus time characteristics

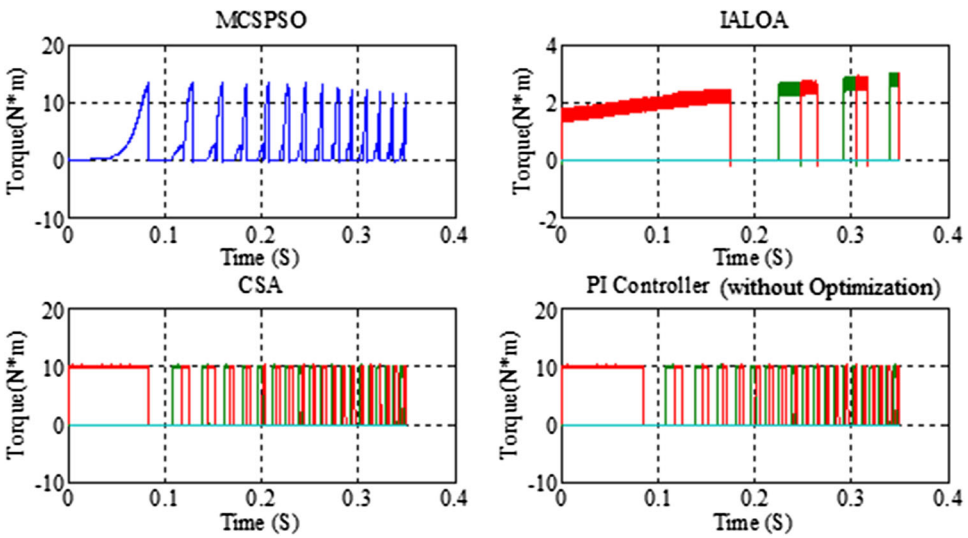

Fig. 22 Torque versus time characteristics

Table 1 Comparison of optimization techniques under single-phase open circuit fault condition

Controller type	T_r (s)	T_p (s)	T_s (s)	E_{ss} (%)
CSA	0.09	0.28	0.50	2.67
IALOA	0.09	0.26	0.28	2.51
MCSPSO	0.09	0.25	0.28	1.26

Table 2 Comparison of optimization techniques under single-phase short circuit fault condition

Controller type	T_r (s)	T_p (s)	T_s (s)	E_{ss} (%)
CSA	0.092	0.275	0.45	2.77
IALOA	0.092	0.245	0.27	2.82
MCSPSO	0.090	0.24	0.25	1.75

Table 3 Comparison of optimization techniques under double-phase open circuit fault condition

Controller type	T_r (s)	T_p (s)	T_s (s)	E_{ss} (%)
CSA	0.097	0.27	0.47	3.27
IALOA	0.094	0.24	0.25	2.81
MCSPSO	0.092	0.23	0.24	1.94

Table 4 Comparison of optimization techniques under double-phase short circuit fault condition

Controller type	T_r (s)	T_p (s)	T_s (s)	E_{ss} (%)
CSA	0.75	0.41	0.42	2.84
IALOA	0.85	0.23	0.23	2.73
MCSPSO	0.078	0.23	0.23	1.89

of 1500 rpm. At first, the external load torque is nil, and the motor is generating only the frictional and winding torques. Figure 27 shows the speed waveform of the SR motor, but the speed waveform is highly oscillatory. This speed waveform shown in Fig. 28 is taken as a test signal for the proposed signal processing approach. The proposed classifier then accurately gives the fault types (Figs. 29, 30, 31, 32, 33).

The performance of the proposed method is contrasted with the existing classification terminologies (CNN and SVM). For a varying number of test samples, our method shows superior performance with a maximum accuracy of 98.3% as shown in Fig. 34. The reliability of the proposed method is assured as the performance is consistently high without any compromise (Table 5).

The sensitivity of the proposed method indicates the true positive value of the SPEED classification. It is measured as the proportion of the actual positive that are correctly classified. The sensitivity performance is more than the existing method with a maximum value of 98%, whereas the maximum sensitivity of CNN and SVM are lies at 93% and 86%. The sensitivity comparison is given in Fig. 35 (Tables 6 and 7 show the sensitivity and specificity comparison).

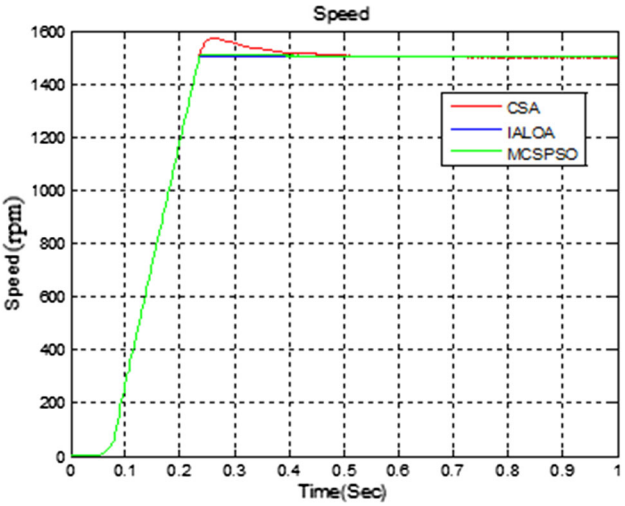

Fig. 23 Speed tracking performance with various algorithms for single-phase open circuit

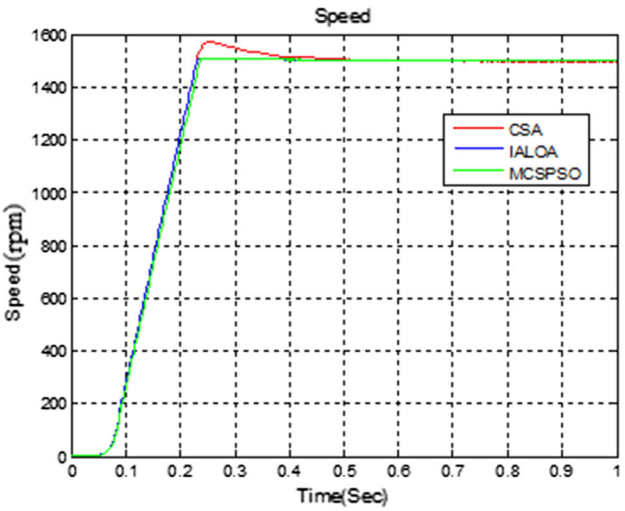

Fig. 24 Speed tracking performance with various algorithms for single-phase short circuit

The specificity values of the proposed method are changing in a zigzag manner as the number of test samples increases with a maximum specificity of 98.2% for the proposed method and 95.6%, 87% for CNN and SVM classifiers. The specificity comparison is given in Fig. 36.

4 Conclusion

Soft computing-based radial basis function neural network was presented for automatic diagnosis and classification of faults in SR motor. The proposed method is effective in iden-

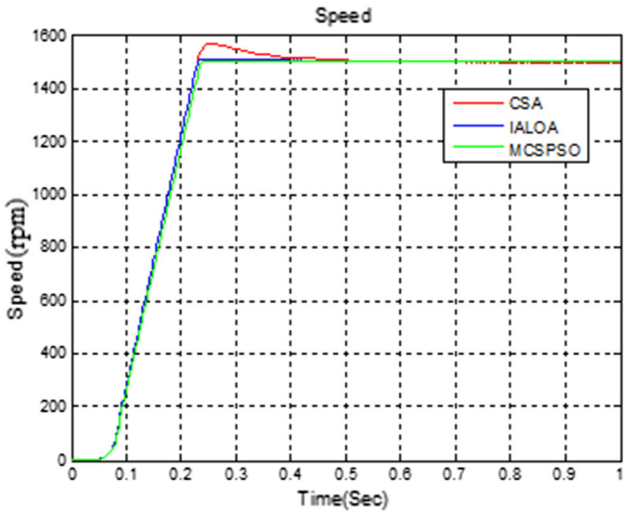

Fig. 25 Speed tracking performance with various algorithms for double-phase open circuit

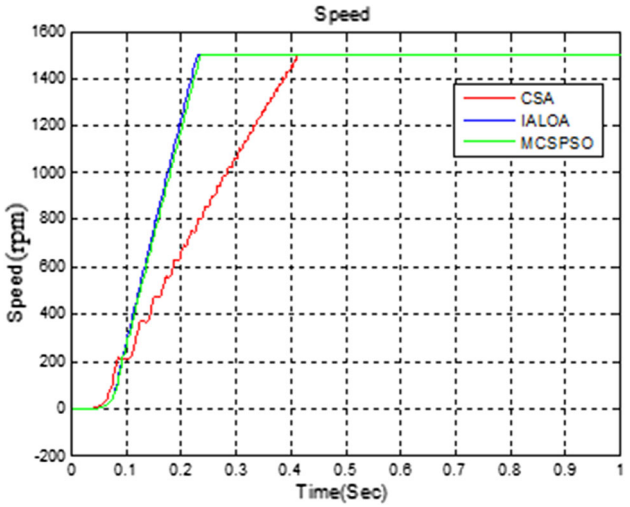

Fig. 26 Speed tracking performance with various algorithms for double-phase short circuit

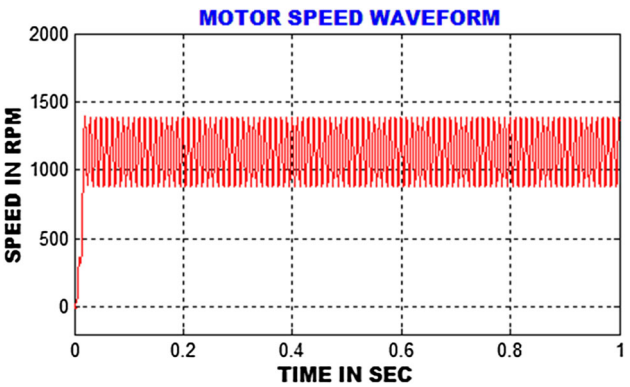

Fig. 27 Unhealthy motor speed waveform

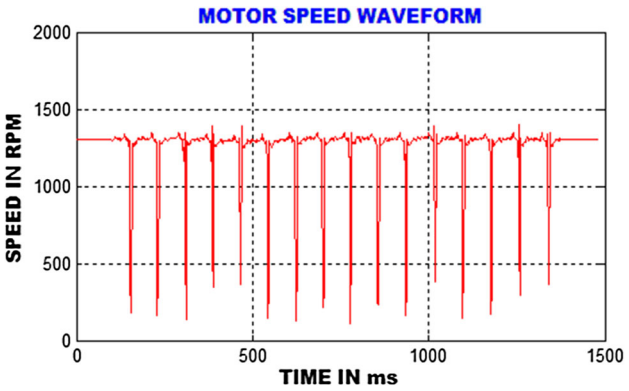

Fig. 28 Speed signal for proposed approach

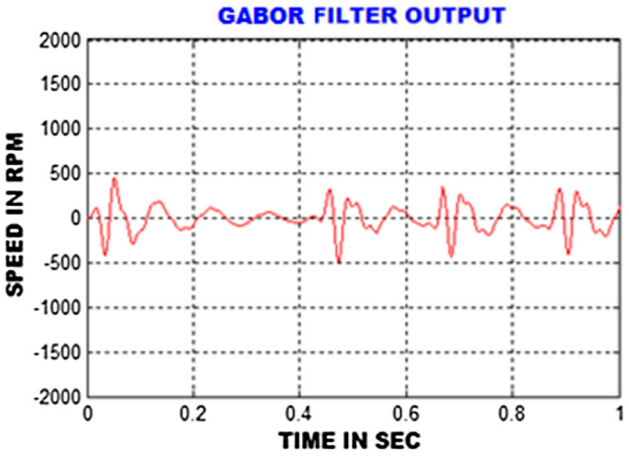

Fig. 29 Preprocessing Gabor filter output signal waveform

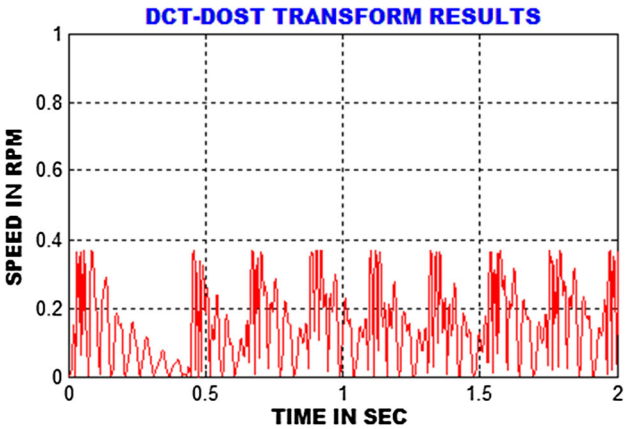

Fig. 30 DCT-DOST transform output waveform

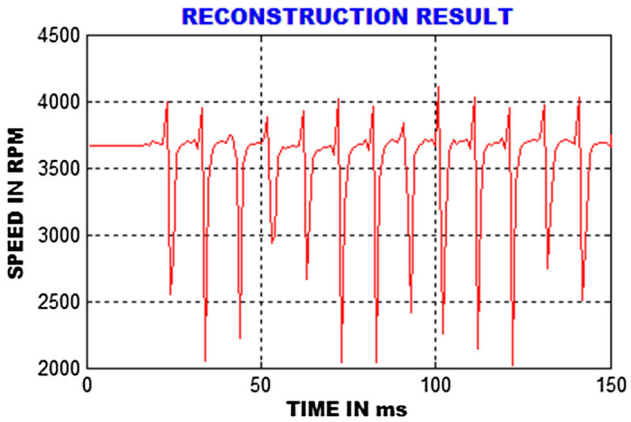

Fig. 31 Reconstruction result waveform

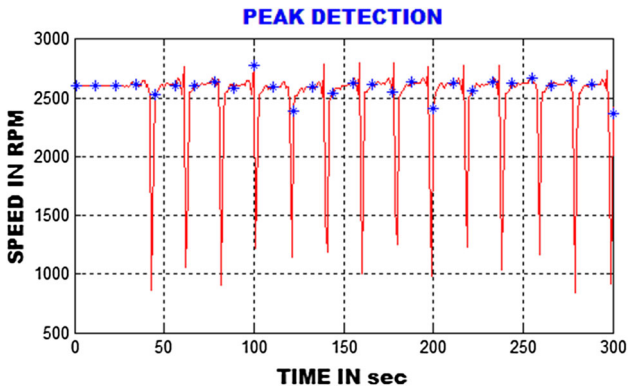

Fig. 32 Peak signal identification result waveform

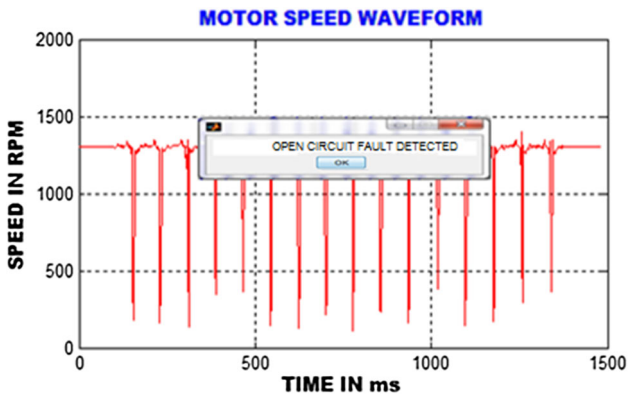

Fig. 33 Classification result using proposed RBFNN classifier

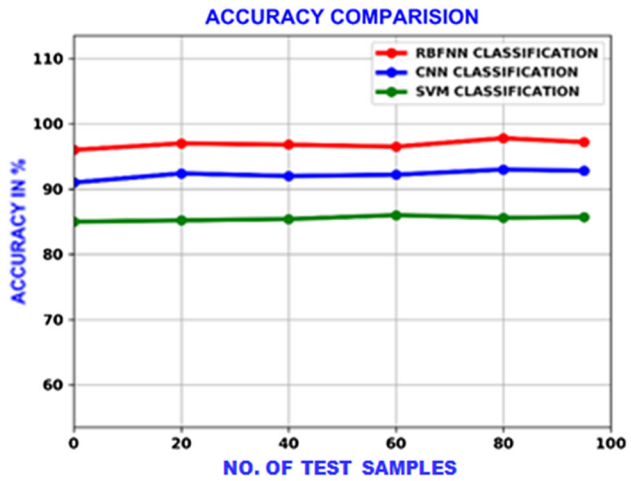

Fig. 34 Accuracy comparison of different methods

Table 5 Accuracy comparison between RBFNN, CNN and SVM

Accuracy comparison table			
No. sample	RBFNN (%)	CNN (%)	SVM (%)
20	95	91	84.5
40	95.5	91.5	84.1
60	95.8	91.4	85
80	97.5	91.8	85.5
100	98.3	92	86

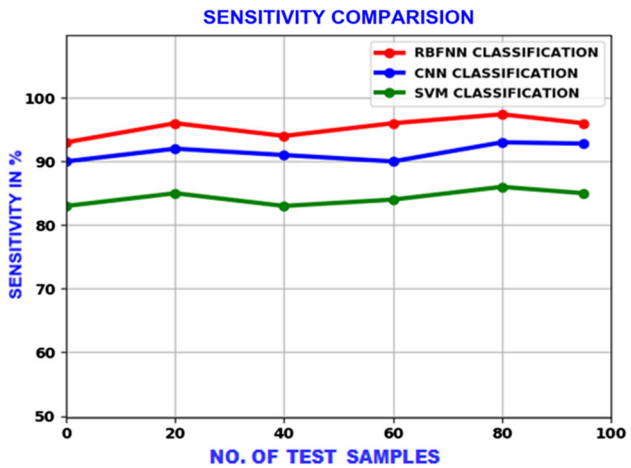

Fig. 35 Sensitivity comparison

tifying any types of faults under any operating mode. The classifier algorithm is trained with numerous experimental speed data that are different from the test speed data used by the algorithm. This would allow the classifier to perform well for any type of motors and faults. The ratio between the upper and lower limit of speed is used as a fault feature to diagnose open circuit and short circuit faults. The reliability of the SR motor drives is improved because of the accurate and rapid fault diagnosis under transient and steady states. The classification performance of the proposed advanced intelligent algorithm is measured in terms of accuracy (98.3%), sensitivity (98%), and specificity (98.2%), which reveals the effectiveness of RBFNN compared with CNN and SVM.

Table 6 Sensitivity comparison between RBFNN, CNN, and SVM

Sensitivity comparison table			
No. sample	RBFNN (%)	CNN (%)	SVM (%)
20	96	91.5	84.5
40	95.3	91	83
60	96.2	90	84.2
80	97.4	92	85
100	98	93	86

Table 7 Specificity comparison between RBFNN, CNN, and SVM

Specificity comparison table			
No. sample	RBFNN (%)	CNN (%)	SVM (%)
20	96	91.5	86.5
40	98.3	93	87
60	97.2	90	87.2
80	99	95	88
100	98.2	95.6	87

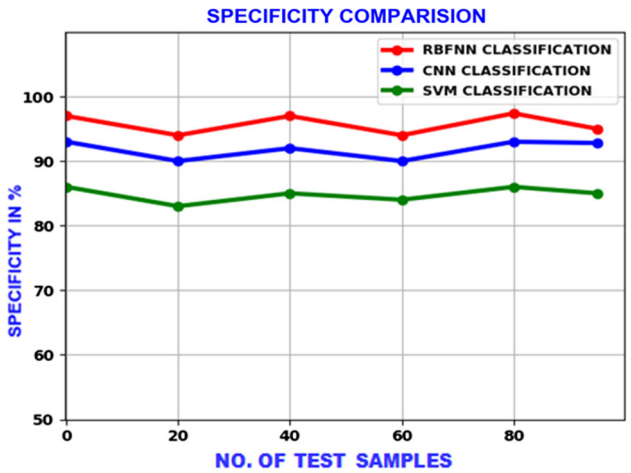

Fig. 36 Comparison of specificity

References

1. Gopalakrishnan, S.; Omekanda, A.M.; Lequesne, B.: Classification and remediation of electrical faults in the switched reluctance drive. IEEE Trans. Ind. Appl. **42**(2), 479–486 (2006)
2. Ruba, M.; Viorel, I.A.; Szabo, L.: Modular stator switched reluctance motor for fault tolerant drive systems. IET Electric Power Appl. **7**(3), 1098–1102 (2013)
3. Ahn, J.-W.; Lukman, G.F.: Switched reluctance motor: research trends and overview. CES Trans. Elect. Mach. Syst. **2**(4), 339–347 (2018)
4. Ilhem, B.; Amar, B.; Lebaroud, A.: Classification method for faults diagnosis in reluctance motors using hidden Markov models. In: IEEE 23rd International Conference on Industrial Electronics (ISIE) (2014)
5. Mir, S.; Islam, M.S.; Sebastian, T.; Husain, I.: Fault-tolerant switched reluctance motor drive using adaptive fuzzy logic controller. IEEE Trans. Power Electron. **19**(2), 289–295 (2004)
6. Huang, X.; Res, G.E.G.; Habetler, N.; Harley, T.G.: Detection of rotor eccentricity faults in a closed-loop drive-connected induction motor using an artificial neural network. IEEE Trans. Power Electron. **22**(4), 1552–1559 (2007)
7. Belfore, L.A.; Arkadan, A.: A methodology for characterizing fault tolerant switched reluctance motors using neuro genetically derived models. IEEE Trans. Energy Convers. **17**(3), 380–384 (2002)
8. Xiao, L.; Sun, H.; Gao, F.; Hou, S.; Li, L.: A new diagnostic method for winding short-circuit fault for SRM based on symmetrical component analysis. Chin. J. Electr. Eng. **4**(1), 74–82 (2018)
9. Liang, J.; Jian, L.; Chang, M.; Xu, G.: A compact integrated switched reluctance motor drive with bridgeless PFC converter. In: IEEE Energy Conversion Congress and Exposition (2013)
10. Gameriro, N.S.; Marques Cardoso, A.J.: A new method for power converter fault diagnosis in SRM drives. IEEE Trans. Ind. Appl. **48**(2), 653–662 (2012)
11. Khwan-on, S.; de Lillo, L.; Empringham, L.; Wheeler, P.: Fault-tolerant matrix converter motor drives with fault detection of open switch faults. IEEE Trans. Ind. Electron. **59**(1), 257–268 (2012)
12. Lu, S.; Chen, H.; Zan, X.: Fault diagnosis and fault-tolerant control strategy for power converter of switched reluctance motor. Trans. China Electro Tech. Soc. **24**(11), 199–206 (2009)
13. Cai, J.; Deng, Z.; Rongguan, H.: Position signal faults diagnosis and control for switched reluctance motor. IEEE Trans. Magn. **50**(9), 1–11 (2014)
14. Sozer, Y.; Husain, I.; Torrey, D.A.: Guidance in selecting advanced control techniques for switched reluctance machine drives in emerging applications. IEEE Trans. Ind. Appl. **51**(6), 4505–4514 (2015)
15. Scelba, G.; De Donato, G.; Pulvirenti, M.; Giulii Capponi, F.; Scarcella, G.: Hall-effect sensor fault detection, identification, and compensation in brushless DC drives. IEEE Trans. Ind. Appl. **52**(2), 1542–1554 (2016)
16. Guo, H.J.; Takahashi, M.; Watanabe, T.; Ichinokura, O.: A new sensorless drive method of Switched Reluctance Motors based on motor's magnetic characteristics. IEEE Trans. Magn. **37**(4), 2831–2833 (2001)
17. Bateman, C.J.; Mecrow, B.C.; Clothier, A.C.: Sensorless operation of an ultra-high-speed switched reluctance machine. IEEE Trans. Ind. Appl. **46**(6), 2329–2337 (2010)
18. Chen, H.; Shengli, L.: Fault diagnosis digital method for power transistors in power converters of switched reluctance motors. IEEE Trans. Ind. Electron. **60**(2), 26–35 (2013)
19. Shao, J.; Deng, Z.; Yu, G.: Fault-tolerant control of position signals for switched reluctance motor drives. IEEE Trans. Ind. Appl. **53**(3), 2826–2839 (2017)
20. Gan, C.; Chen, Y.; Qu, R.; Yu, Z.; Kong, W.; Hu, Y.: An overview of fault-diagnosis and fault-tolerance techniques for switched reluctance machine systems. In: IEEE Access (2019)
21. Buccella, C.; Cecati, C.; Latafat, H.: Digital control of power converters—a survey. IEEE Trans. Ind. Inform. **8**(3), 437–447 (2012)
22. Li, H.; Li, W.; Ren, H.: Fault-tolerant inverter for high-speed low inductance BLDC drives in aerospace applications. IEEE Trans. Power Electron. **32**(3), 2452–2463 (2017)

23. Lu, J.; Hu, Y.; Liu, J.: Analysis and compensation of sampling errors in TPFS IPMSM drives with single current sensor. IEEE Trans. Ind. Electron. **66**(5), 3852–3855 (2019)
24. Khan, M.A.S.K.; Radwan, T.S.; Rahman, M.A.: Real-time implementation of wavelet packet transform-based diagnosis and protection of three-phase induction motors. Energy Convers. IEEE Trans. Energy Convers. **22**(3), 647–655 (2007)
25. Hoseini, S.R.K.; Farjah, E.; Ghanbari, T.; Givi, H.: Extended Kalman filter-based method for inter-turn fault detection of the switched reluctance motors. IET Electric Power Appl. **10**(8), 714–722 (2016)
26. Uysal, A.; Bayir, R.: Real-time condition monitoring and fault diagnosis in switched reluctance motors with Kohonen neural network. J. Zhejiang Univ. Sci. C (Comput. Electron.) **14**, 941–952 (2013)